Kinetics of non-oxidative propane dehydrogenation on Cr_2O_3 and the nature of catalyst deactivation from first-principles simulations

Matej Huš, Drejc Kopač, and Blaž Likozar*

Department of Catalysis and Chemical Reaction Engineering, National Institute of Chemistry, Hajdrihova 19, SI-1000 Ljubljana, Slovenia

E-mail: blaz.likozar@ki.si

Abstract

As the global demand for propene (propylene) is increasing, classic commercial production processes are becoming unable to keep up. Non-oxidative dehydrogenation, although hitherto underutilised industrially, has been put forward as a viable and green alternative, which is already used in a few commercial processes. In this work, we present detailed first-principles calculations of this reaction over a chromium oxide catalyst, which is the cornerstone of the CATOFIN® process. A complete reaction pathway for the dehydrogenation of propane to propene and ultimately to propyne (methylacetylene) was considered. Cracking, which can yield C_1 and C_2 hydrocarbons, and the deactivation of the catalyst because of coking were also included and modelled. We used density functional theory calculations with the Hubbard model to study the structure of the involved intermediates, their adsorption and their interconversion to explain how chromium oxide catalysts facilitate this reaction and which processes cause

their deactivation. We showed that the interaction of the hydrocarbons and molecular hydrogen with the catalytic surface is rather weak, resulting in low surface coverages, but increasing with multiple bonds present in hydrocarbons. Having constructed the potential energy surface with all the intermediates and the transition states linking them, we proposed a kinetic model for the reaction. Kinetic Monte Carlo simulations were performed at experimentally relevant temperatures (700–1000 °C), pressures (up to 10 bar) and inlet mixture compositions to study the kinetics of the reaction and discover the rate determining steps. As the reaction is highly endothermic, considerable conversions only occur at high temperatures. The accumulation of propene and propyne in the reaction mixture adversely affects the reaction rate and selectivity. Higher pressures increase the reaction rate but also increase the rate of coke formation, which poisons the catalyst. Deactivation of the catalyst has a strong temperature dependence and is caused by the accumulation of C^* and CH_3CC^* on the surface, which are hard to remove even with hydrogen.

Keywords

Dehydrogenation, chromium oxide, propane, DFT/KMC, kinetics.

Introduction

Increased global demand for energy, which is still produced mostly from fossil fuels, has been responsible for a positive trajectory of the global CO_2 emissions.[1] It is therefore of paramount importance to develop improved catalysts and catalytic processes, which require less energy. Also increasing is the demand for light alkenes, such as propene and butadiene. Propene is, for instance, the second most important precursor chemical in the petrochemical industry, being used in the production of plastics (polypropylene), propylene oxide, acrylic acid and acrylonitrile.

2

Propene has been traditionally produced in petroleum refineries with steam cracking and fluid catalytic cracking.[2] These processes have been unable to keep up with the increased demand for propene, prompting the development of catalytic processes using other sources. Dehydrogenation of propane, which is an abundant by-product of petroleum refining and natural gas processing, is a commonly used alternative.[3–7] Using propane as a raw material and not a fuel feedstock in the current petroleum refining process also contributes to a greener and more sustainable use of natural resources.[8] As a side product, hydrogen is also produced.[9,10]

Propane valorisation represents a technological challenge due to the inertness of the reactant and quick deactivation of the catalyst.[11] In non-oxidative dehydrogenation, hydrogen and light olefins are formed in a very endothermic reaction. For instance, the enthalpy of the reaction $C_3H_8 \rightarrow C_3H_6 + H_2$ is 124 kJ mol^{-1}. According to Le Chatelier's principle, the reaction is favoured at high temperatures and low pressures (due to a positive change in entropy). Industrially, propane dehydrogenation is carried out mainly with two competing processes. For the OLEFLEX® process, alumina-supported Pt/Sn catalysts at 800–1000 K and 2–4 bar are used, yielding a 20–70 % conversion.[12,13] Often, Sn can be doped[14] or substituted altogether.[15] However, more commonly used is the CATOFIN® process, where chromium oxide catalysts on alumina support are used. The reaction proceeds at 850 K and 1.2 1.5 bar, yielding propene with a 60-70 % conversion in the steady state.[16] This method is advantageous as it uses no critical or expensive raw materials (such as noble metals). A drawback of both processes is coking, which requires frequent catalyst regeneration or change. Experimental and theoretical treatment of this reaction is warranted in the quest towards better activity, higher selectivity, less coking and improved longevity.

Despite extensive experimental research,[17] theoretical insight is lacking or focuses on phenomenological mathematical simulations.[18–20] Surprisingly, theoretical research has focused disproportionately on the OLEFLEX® process. Several density functional theory (DFT) studies have been performed to study the thermodynamics and kinetics of the reaction on

3

stepped Pt surfaces,[21] Pt nanoparticles,[22] Pt clusters,[23] PtSn particles,[24] and PtSn surfaces.[25] Studies on the problem of coking have, unsurprisingly, focused on simple surfaces, such as Pt(111).[26,27] Studies on Pt_3Sn have shown that tin decreases the adsorption interaction of propane and propene,[28] which has an advantageous effect on the selectivity.[29]

The chromium oxide process has garnered much less attention. Based on extensive experimentation, Suzuki and Kaneko postulated an empirical kinetic model[30] without breaking down the reaction into elementary steps. Chang *et al.* studied the catalytic behavior of α-$Cr_2O_3(0001)$ and $ZnO(10\bar{1}0)$ in propane dehydrogenation, showing a positive effect of Pt doping.[31] Experimentally, Zhang *et al.* studied the reaction on mesoporous SBA-15-supported chormium oxide.[32] The type of alumina support and the amount of acid sites were shown to have a marked effect on activity.[33] Shee and Sayari showed that mesoporous Cr_2O_3/Al_2O_3 catalysts exhibit high activity with significant interconversion between Cr(III) and Cr(VI) during the reaction.[34] Nijhuis *et al.* performed an *operando* spectroscopic analysis of the process to study the dynamics of the catalyst.[35] There have been a few kinetic studies, but none described the process with the rigour of including elementary reactions.[36,37]

Little theoretical insight has been provided into the reaction. In this work, we therefore study the adsorption of reactants and products (hydrogen, propane, propene, propyne) and their transformations on $Cr_2O_3(0001)$ using first-principle methods. A full reaction network of non-oxidative dehydrogenation, ultimately yielding propyne, is postulated and its thermodynamic and kinetic parameters calculated *ab initio*. Without any *a priori* limitations, we allow all possible reaction steps, specifically including cracking and coking reactions. These data are used in a kinetic model via the kinetic Monte Carlo (kMC) method to predict the reaction rates at various conditions. We identify the reaction steps leading to intermediates, which either represent mechanistic dead ends (such as CH_3CC^* or C^*) or are prone to cracking and eventual coke formation. The effects of temperature, pressure, and hydrogen, olefins and small hydrocarbon contaminants are investigated. The rate-determining steps are identified for the desired reaction (propene formation) and side reactions (light hydrocarbons

4

formation and coking).

The results show that at low temperatures propene is formed from propane with high selectivity but with a low turnover frequency and an apparent activaton barrier 1.37 eV. As the temperature is increased, cracking and coking become more important. Kinetic modelling of coking show that the deactivation of the catalyst is primarily due to the formation of CH_3CC^* and C^*, which poison it. Cracking occurs when the C–C bond is broken in predominantly $CH_3CH_2CH_2^*$ and to a lesser extent in CH_3CHCH^*. The reaction rate is considerably lowered when propene or propyne are allowed to accumulate, decreasing both selectivity and activity.

Computational details

First-principles calculations

We performed the DFT calculations with the VASP package,[38–41] which uses the plane-wave formalism to incorporate the periodic bounday conditions. To describe the semilocal exchange and correlation, the Perdew-Wang 91 approach was used,[42] while for the electron-core interaction the project augmented wave method was employed.[43,44] All calculations were performed in a spin-polarized fashion. Based on convergence testing, the energy cut-off of 500 eV was chosen. Due to a significant self-interaction error when treating Cr with simple GGA pseudopotentials, the Hubbard $+U$ correction for the $3d$ states of Cr was used (DFT+U).[45] Based on an extensive literature review, we opted for the values $D = 5\,\mathrm{eV}$ and $J = 1\,\mathrm{eV}$.[46,47] The PW91 functional with these DFT+U parameters has been shown to yield results that match experiments.[48,49] To account for the dispersion interaction, the Grimme D3 method was employed.[50] The force threshold for the determination of intermediates and transition states was selected to be 0.03 eV/Å. Preliminary testing showed that refining to 0.01 eV/Å offered marginal improvements ($\Delta E \leq 0.04$ eV), which are smaller than the accuracy of the DFT method itself. The transition states were roughly identified with

5

the nudged elastic band method[51] and further refined with the dimer method.[52–55] For vibrational analysis, the finite difference approach with a displacement of 0.01 Å sufficed. Zero-point energy corrections were included.

Since a unit cell of Cr_2O_3 consists of 30 atoms and is rather large, a $4\times4\times2$ Monkhorst–Pack mesh of k points was used. The cell-size optimization yielded the cell constants $a_0 = 5.09$ Å and $c_0 = 13.77$ Å, which is consistent with the experimental values ($a = 5.00$ Å and $c_0 = 13.59$ Å) within 2 %. When cut along the (0001) surface, the slab was modeled with 12 alternating layers of Cr and O atoms (six each), as shown in Figure 1. This yielded a mixed Cr-O surface termination, which is in line with the experimental observations of autoreducing and the presence of mono-oxo species.[56] The bottom six layers were frozen into their bulk positions, while the top layers and the adsorbates were free to relax. On account of a relatively large 2×2 supercell ($2a_0 = 10.18$ Å), the Γ point sampling was adequate. The slabs were separated by 15 Å of vacuum in the z-direction. Spurious interslab interactions were remedied using the standard dipole correction.[57,58]
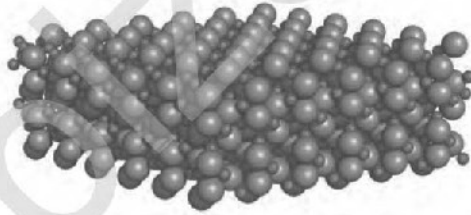

Figure 1: Perspective view of the twelve-layered Cr_2O_3 (0001) catalytic surface. Colour code: red – oxygen, violet – chromium.

The adsorption energies were evaluated as $E_{ads} = E_{adsorbed} - E_{adsorbate} - E_{slab}$, where $E_{adsorbed}$ represents the energy of a fully relaxed slab with the adsorbate, $E_{adsorbate}$ is the energy of a fully relaxed gaseous adsorbate and E_{slab} is the energy of a fully relaxed empty slab. We can decompose the adsorption energy into the electronic interaction, E_{int} and the distortion energies of the slab and the adsorbate, $E_{surf,dis}$ and E_{dis}, respectively. Their sum equals the adsorption energy.

$$E_{surf,dis} = E_{slab} - E_{slab}^{\infty} \tag{1}$$

$$E_{dis} = E_{adsorbate} - E_{adsorbate}^{\otimes} \tag{2}$$

$$E_{int} = E_{adsorbed} - E_{slab}^{\otimes} - E_{adsorbate}^{\otimes}, \tag{3}$$

where $\otimes$ represents that the molecule or slab have the same geometry as in the fully relaxed adsorbed state.

Kinetic parameters

When studying heterogenous catalytic reactions, there are several different processes. For surface reactions, the forward rate constant follows the Arrhenius equation:

$$k_{fwd} = \frac{Q_{vib}^{\sharp}}{Q_{vib}^{R}} \frac{k_B T}{h} \exp\left(-\frac{E_{fwd}}{k_B T}\right), \tag{4}$$

with Q_{vib} being the vibration partition function of the reactants and the transition state, k_B the Boltzmann constant, T temperature, h the Planck constant, and E_{fwd} the activation barrier. For the reverse reactions, we substitute the reactants for products and arrive at

$$k_{rev} = \frac{Q_{vib}^{\sharp}}{Q_{vib}^{P}} \frac{k_B T}{h} \exp\left(-\frac{E_{rev}}{k_B T}\right), \tag{5}$$

where barring any lateral interactions the identity $E_{fwd} - E_{rev} - \Delta E$ must hold.

For the surface reactions involving a gaseous species (ER reactions), we have to account for the rotational and translational partition function of the said species:

$$k_{fwd} = \frac{Q_{vib}^{\sharp}}{Q_{vib}^{lat} Q_{vib}^{gas} Q_{rot}^{gas} Q_{trans}^{gas}} \frac{pA}{\sqrt{2\pi m k_B T}} \exp\left(-\frac{E_{fwd}}{k_B T}\right), \tag{6}$$

with p being the pressure, A the effective area of the reaction site and m the mass. Dissociative adsorption of hydrogen can be considered an ER reaction. Non-activated adsorption

is a special case of this mechanism with $E_{fwd} = 0$. This makes it a kinetic event:

$$k_{fwd} = \frac{pA}{\sqrt{2\pi m k_B T}},\tag{7}$$

while the reverse reaction (desorption) follows Eq. 6. In all cases, the partition functions are calculated from the harmonic approximation.

Kinetic Monte Carlo simulations

The reaction mechanism and kinetic parameters from the DFT calculations were fed into a kinetic Monte Carlo simulation. These were used to elucidate the dynamics of the reaction on a mesoscopic scale, including theoretical estimates of the apparent activation barrier, turnover frequencies (TOFs), selectivity and production rates under different relevant conditions. We used the software package *Zacros*, which employs a graph-theoretical approach. The Hamiltonian of a particular lattice configuration follows from the energetic model, which takes into account the number of figures or clusters and their interactions if relevant. More technical details on the method have been published elsewhere.[59–62]

We ran the calculations on a hexagonal lattice with two types of active sites, corresponding to oxygen atoms (for binding the hydrogen atom) and chromium atoms (for the hydrocarbons), totaling 800 sites ($2 \cdot 20 \times 20$). Based on the DFT data, each species was treated as monodentate, occupying one active site. For each set of conditions, four simulations with differing seeds were executed and averaged. The simulations were set up with no pre-bound adsorbates on the lattice and run for 10^7 events. Testing the simulations on a smaller lattice with a shorter wall time proved that this is sufficient to obtain equilibrated results. Adsorption and diffusion reactions had their forward and reverse constant scaled down to avoid wasting computational time. By making sure that their ratio remains the same, this approach has no net effect on the equilibrium concentrations. This stiffness scaling approach has been tested before.[63]

8

Results and discussion

Ab initio calculations

Adsorption

Propane is a member of the family of saturated hydrocarbons, which are notable for their strong bonds and low interaction with other molecules or surfaces. This is evidenced in both, high barriers for its activation (necessitating high temperatures) and low adsorption energy. Even when specifically including the van der Waals interaction through semi-empirical corrections, which DFT itself is notoriously bad at, the adsorption energy is merely -0.36 eV. Propane physisorbs non-specifically; the potential energy surface of the adsorption is very flat and the energy does not change significantly (≤ 0.05 eV) when the adsorbate is translated along the surface. Therefore, six different positions for propane adsorption were tested. On the contrary, propene and propyne interact more strongly with the surface and occupy well-defined sites on the catalyst (on top of the Cr atoms interacting with the π electrons of the double bond). They preferably bind to the top site of chromium atoms with the multiple bond. In Figure 2, we show their positions in more detail. Another measure of the binding strength is the charge density difference upon the adsorption as compared to the isolated molecules and adsorbates, which we depict in Figure 3, superimposed on a slab (the adsorbate molecule is omitted from the plot). We notice that the charge density is much less perturbed in the case of propane, which results in weaker binding.

Molecular hydrogen, however, does not bind substantially to the surface. Hydrogen atoms, resulting from the dehydrogenation reaction itself, reside on the oxygen atoms, while the binding to Cr is energetically unfavourable. Upon recombination, they leave the surface as H_2.

In Table 1, we list the adsorption energies of propane, propene, propyne, ethane, ethene, ethyne, methane and hydrogen. They can be decomposed into the (generally negative) interaction energy, which describes the strength of the electronic interaction between the
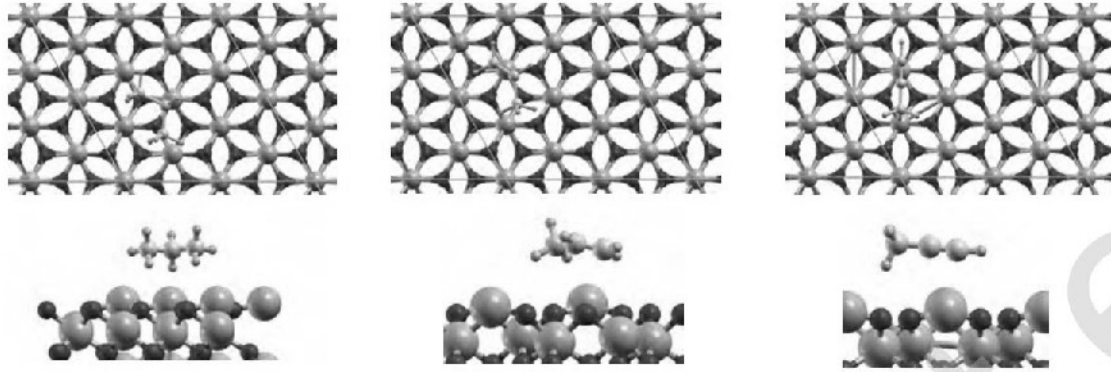
9

Figure 2: Geometries of the adsorption of propane (left), propene (center) and propyne (right) in a top and side view.
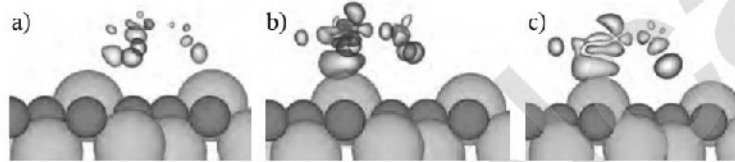

Figure 3: Charge density difference, $\Delta\rho\left(\mathbf{r}\right) = \rho_{adsorbed}\left(\mathbf{r}\right) - \rho_{adsorbate}\left(\mathbf{r}\right) - \rho_{slab}\left(\mathbf{r}\right)$, for a) propane, b) propene, and c) propyne. Red (blue) color represents electron charge excess (deficit) regions. The scale is consistent (contours at $0.0015\ e_0/\text{Å}^3$).

adsorbate and the surface, and the (positive) distortion energy of the surface and adsorbate, which describes the unfavorable contribution due to the geometrical distortion of the surface and adsorbate. The latter effect is shown to be miniscule ($\leq 0.04\,\mathrm{eV}$) and completely eclipsed by the electronic interaction.

Table 1: Adsorption energies for stable compounds in the reaction scheme can be decomposed into the interaction and distortion energy. All values are in eV.

species	$E_{surf,dis}$	E_{dis}	E_{int}	E_{ads}
C_3H_8	0.00	0.02	-0.38	-0.36
$CH_3CH{=}CH_2$	0.03	0.02	-0.50	-0.45
$CH_3C{\equiv}CH$	0.04	0.02	-0.69	-0.63
C_2H_6	0.00	0.02	-0.25	-0.23
$CH_2{=}CH_2$	0.02	0.02	-0.43	-0.39
$CH{\equiv}CH$	0.04	0.02	-0.46	-0.40
CH_4	0.00	0.01	-0.15	-0.14
H_2	0.00	0.00	-0.04	-0.04

10

Reaction mechanism

The mechanism of non-oxidative propane dehydrogenation can be described with elementary reaction steps, which we divide into three groups: (*i*) adsorption/desorption, (*ii*) diffusion and (*iii*) surface reactions. There are eight components (molecular H_2 and all stable C_1, C_2, and C_3 hydrocarbons) that can physisorb in a non-activated fashion. Molecular hydrogen binds very weakly and non-specifically to the catalyst (-0.04 eV). Thus, its subsequent dissociation can be rather viewed as an Eley-Rideal reaction (non-activation adsorption) than a surface (Langmuir-Hinshelwood) reaction. The adsorption of the stable hydrocarbons (*vide supra*) is non-activated. Diffusion of the hydrogen atoms is included because the adsorption energy of hydrogen is significant. The diffusion barrier for the hydrogen atom is 0.61 eV, which is comparable to its desorption energy. Other species are either bound too strongly (immobile) or too weakly to require the inclusion of adsorption. For instance, hydrocarbons bind rather weakly to the surface and would have diffusion barriers similar to the energy of desorption. Unstable intermediates such as $CH_3CH_2CH_2$ and others are bound so strongly that their diffusion is slower than the rate of further conversion. Technically, the inclusion of adsorption of these compounds is not necessary because all elementary reaction steps include atomic hydrogen, which is a mobile well-equilibrated species.

Other surface reactions are grouped according to the chemical "meaning" of the reaction. The reactions that cleave a hydrogen atom, resulting in stable intermediates or monoradicals, are deemed dehydration reactions. By following these reactions in the pathway, dehydrogenation follows an orderly sequence (propane $\rightarrow$ propene $\rightarrow$ propyne). Deep dehydrogenation reactions involve diradicals or species that cannot lead to stable products. The reactions where C–C bonds break are called cracking reactions. Only cracking reactions with $\Delta E < 3$ eV are used in the model.

In Figure 4, the mechanism of propane dehydrogenation is shown. Propane adsorbs rather non-specifically and undergoes a hydrogen atom abstraction. In this step, it is roughly equally likely for each of the hydrogen atoms to be abstracted by the neighboring oxygen
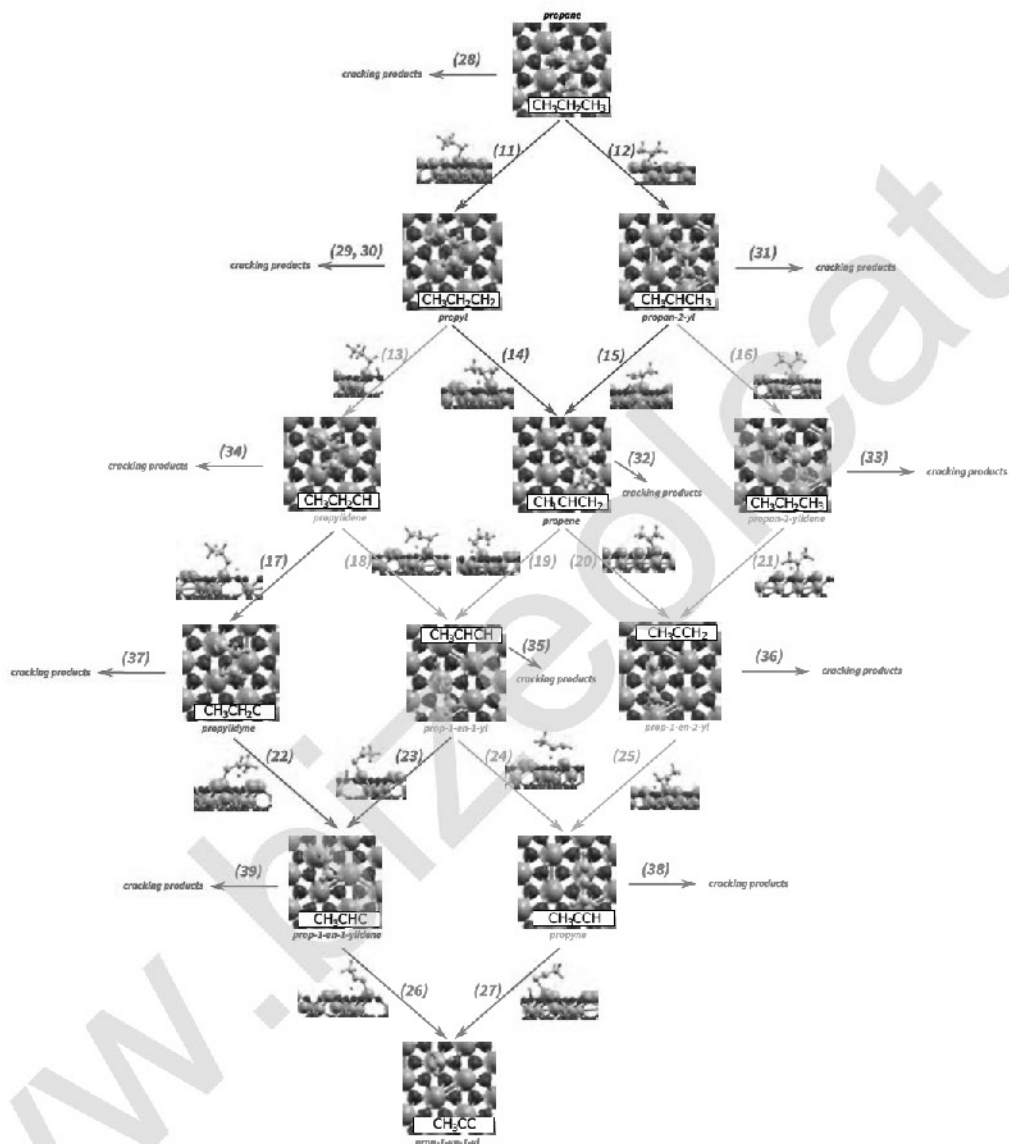
11

Figure 4: Reaction mechanism (surface reactions only) for the C_3 reactions in propane dehydrogenation. Stable structures shown in a top-down view, transition states in a perspective. Reactions numbered as in Table 2. Colour code: propane route (green), propyne route (orange), cracking and coking (red).
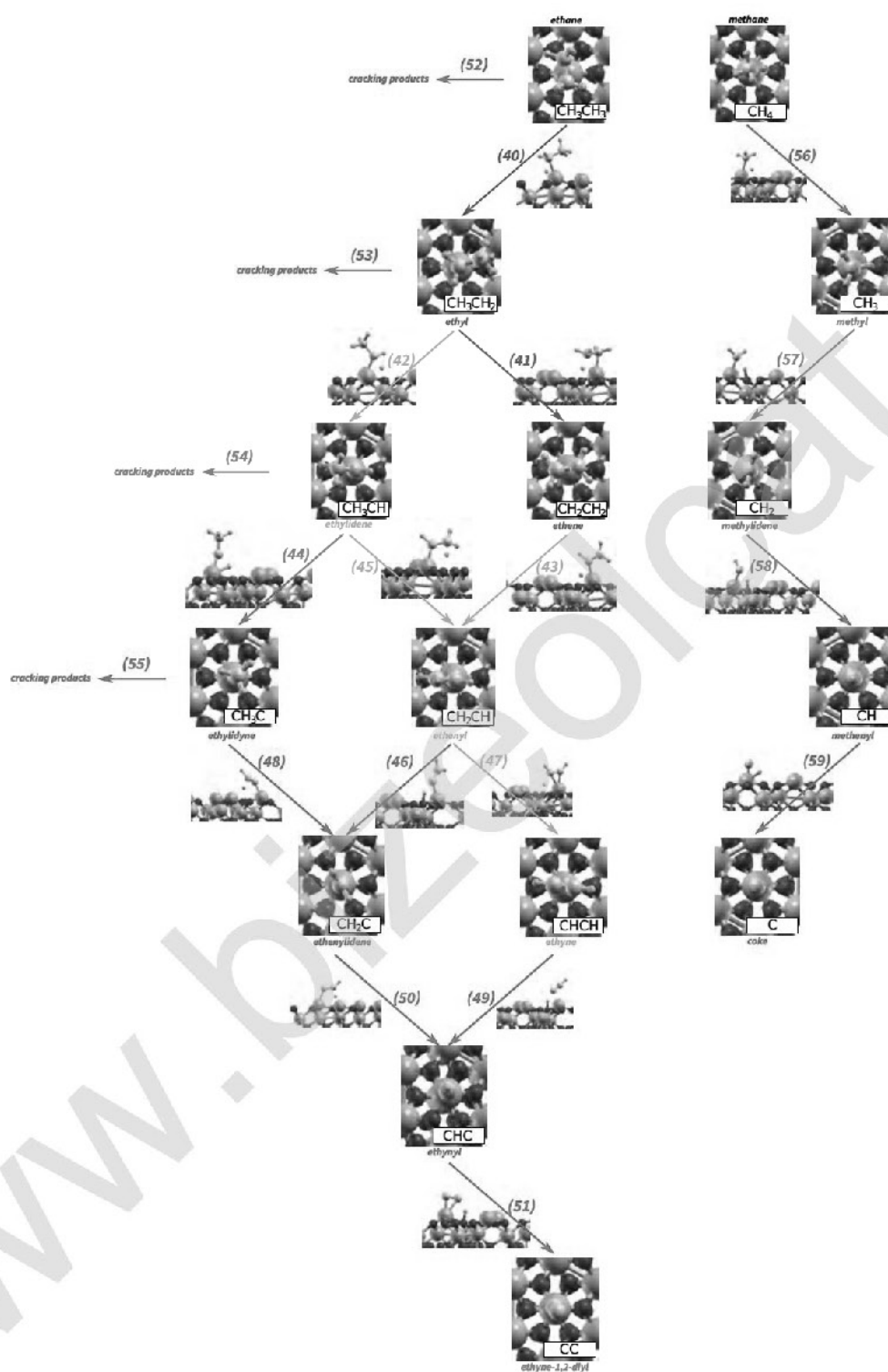
Figure 5: Reaction mechanism (surface reactions only) for the C_2 and C_1 reactions in propane dehydrogenation. Stable structures shown in a top-down view, transition states in a perspective. Reactions numbered as in Table 2. Colour code: ethene route (green), ethyne route (orange), cracking and coking (red).

atom, yielding a hydroxyl group. The barrier for the removal of the methyl hydrogen is 1.25 eV and for the removal of the methylene hydrogen is 1.27 eV. The latter is somewhat less endothermic (+0.73 eV *vs.* +0.85 eV). Following the removal of another hydrogen atom, propene is formed. It is much easier for CH_3CHCH_3 to shed another hydrogen atom ($E_A = 0.83$ eV) than for $CH_3CH_2CH_2$ ($E_A = 1.37$ eV). As shown later in the kinetic analysis, this leads the reaction through the CH_3CHCH_3 pathway. Both secondary steps are almost thermoneutral. However, $CH_3CH_2CH_2$ is much more prone to cracking.

Further dehydrogenation of propene follows a similar mechanism. In this case, the hydrogen atom from the middle carbon atom is again more readily removed ($E_A = 1.22$ eV) than from the terminal carbon atom ($E_A = 1.42$ eV). Subsequent dehydrogenation of CH_3CCH_2 is also more favorable ($E_A = 1.31$ eV) than of CH_3CHCH ($E_A = 1.81$ eV). This reaction proceeds thus almost completely through the CH_3CCH_2 intermediate. Any CH_3CHCH that is formed can undergo a cracking reaction.

In general, deep dehydrogenations have much higher activation barriers. For instance, it is for $\Delta E_A = 0.51$ eV less prboable for $CH_3CH_2CH_2$ to convert to CH_3CH_2CH than to propene (CH_3CHCH_2). However, as shown later on in the kinetic analysis, these reactions serve an important function. First, they serve as conduits to the inactive intermediates, such as CH_3CC^* or C^*, which poison the catalyst surface and do not convert further. Secondly, deep hydrogenations can produce fragments which readily undergo cracking. This latter function is not exclusive as stable intermediates or monoradicals can also fragment. CH_3CCH_2 has the lowest barrier for fragmentation ($E_A = 1.68$ eV), comparable to dehydrogenation reactions, followed by that of $CH_3CH_2CH_2$ ($E_A = 2.32$ eV). The ensuing fragments enter the C_1 and C_2 reaction pathways, which are shown in Figure 5. In the C_2 pathway, ethyne and ethene are predominantly formed. Deep dehydrogenations are less likely in this pathway, as well.

See Table 2 for the kinetic parameters of all the investigated reaction steps. In Figure 6, a graphical representation of the potential energy surface for the C_3 pathway without the deep dehydrogenations is shown. We see that all reaction steps are endothermic.

14

Table 2: Thermodynamic and kinetic parameters of the elementary reactions in the model. Asterisks and (*) and hash signs (#) denote empty lattice sites for the adsorption of hydrocarbons and hydrogen atoms, respectively. Fast-equilibrated steps are indicated by the ampersand sign (&).

¶ Reaction energies are relative to infinitely separated reactants and/or products.

|	reaction step	type	E_A (eV)	ΔE (eV)¶	$k_{fwd}^{850\ K}$ (s^{-1})	$k_{rev}^{800\ K}$ (s^{-1})
1&	$H_2(g) + 2\# \rightarrow H_2\#\#$	ads.	0	−0.04	$p \cdot 1.48 \cdot 10^{9}$	$1.23 \cdot 10^{13}$
2&	$C_3H_8(g) + * \rightarrow C_3H_8*$	ads.	0	−0.37	$p \cdot 3.15 \cdot 10^{8}$	$8.23 \cdot 10^{15}$
3&	$CH_3CH{=}CH_2(g) + * \rightarrow CH_3CHCH_2*$	ads.	0	−0.45	$p \cdot 3.22 \cdot 10^{8}$	$1.02 \cdot 10^{15}$
4&	$CH_3C{\equiv}CH(g) + * \rightarrow CH_3CCH*$	ads.	0	−0.61	$p \cdot 3.30 \cdot 10^{8}$	$1.72 \cdot 10^{15}$
5&	$CH_3CH_3(g) + * \rightarrow CH_3CH_3*$	ads.	0	−0.23	$p \cdot 3.81 \cdot 10^{8}$	$1.55 \cdot 10^{14}$
6&	$CH_2{=}CH_2(g) + * \rightarrow CH_2CH_2*$	ads.	0	−0.39	$p \cdot 3.95 \cdot 10^{8}$	$8.02 \cdot 10^{14}$
7&	$CH{\equiv}CH(g) + * \rightarrow CHCH*$	ads.	0	−0.40	$p \cdot 4.10 \cdot 10^{8}$	$1.53 \cdot 10^{14}$
8&	$CH_4(g) + * \rightarrow CH_4*$	ads.	0	−0.14	$p \cdot 5.22 \cdot 10^{8}$	$4.24 \cdot 10^{12}$
9	$H_2\#\# \rightarrow 2H\#$	dis.	0.54	−0.83	$5.16 \cdot 10^{10}$	$1.00 \cdot 10^{13}$
10&	$H\# + \# \rightarrow \# + H\#$	diff.	0.61	0	$1.04 \cdot 10^{13}$	$1.04 \cdot 10^{13}$
11	$C_3H_8* + \# \rightarrow CH_3CH_2CH_2* + H\#$	dehydr.	1.25	+0.85	$6.14 \cdot 10^{11}$	$9.58 \cdot 10^{12}$
12	$C_3H_8* + \# \rightarrow CH_3CHCH_3* + H\#$	dehydr.	1.27	+0.73	$1.34 \cdot 10^{12}$	$9.15 \cdot 10^{12}$
13	$CH_3CH_2CH_2* + \# \rightarrow CH_3CH_2CH* + H\#$	deep	1.88	+1.59	$1.55 \cdot 10^{13}$	$4.03 \cdot 10^{12}$
14	$CH_3CH_2CH_2* + \# \rightarrow CH_3CHCH_2* + H\#$	dehydr.	1.37	+0.04	$5.30 \cdot 10^{12}$	$1.75 \cdot 10^{11}$
15	$CH_3CHCH_3* + \# \rightarrow CH_3CHCH_2* + H\#$	dehydr.	0.84	+0.16	$3.10 \cdot 10^{10}$	$2.34 \cdot 10^{11}$
16	$CH_3CHCH_3* + \# \rightarrow CH_3CCH_3* + H\#$	deep	1.74	+1.44	$1.99 \cdot 10^{13}$	$6.26 \cdot 10^{12}$
17	$CH_3CH_2CH* + \# \rightarrow CH_3CH_2C* + H\#$	deep	1.87	+1.62	$2.58 \cdot 10^{12}$	$8.00 \cdot 10^{12}$
18	$CH_3CH_2CH* + \# \rightarrow CH_3CHCH* + H\#$	deep	1.79	−0.64	$1.08 \cdot 10^{13}$	$7.71 \cdot 10^{12}$
19	$CH_3CHCH_2* + \# \rightarrow CH_3CCH_2* + H\#$	dehydr.	1.42	+0.90	$3.19 \cdot 10^{11}$	$1.79 \cdot 10^{13}$
20	$CH_3CHCH_2* + \# \rightarrow CH_3CCH_2* + H\#$	dehydr.	1.22	+0.82	$1.25 \cdot 10^{12}$	$2.25 \cdot 10^{13}$
21	$CH_3CCH_3* + \# \rightarrow CH_3CCH_2* + H\#$	deep	0.64	−0.46	$8.48 \cdot 10^{11}$	$3.67 \cdot 10^{12}$
22	$CH_3CH_2C* + \# \rightarrow CH_3CHC* + H\#$	deep	0.30	−0.59	$1.56 \cdot 10^{13}$	$5.55 \cdot 10^{12}$
23	$CH_3CHCH* + \# \rightarrow CH_3CHC* + H\#$	deep	1.42	+1.68	$3.81 \cdot 10^{11}$	$5.91 \cdot 10^{12}$
24	$CH_3CHCH* + \# \rightarrow CH_3CCH* + H\#$	dehydr.	1.81	+0.37	$4.90 \cdot 10^{13}$	$7.42 \cdot 10^{12}$
25	$CH_3CCH_2* + \# \rightarrow CH_3CCH* + H\#$	dehydr.	1.31	+0.45	$8.46 \cdot 10^{12}$	$3.98 \cdot 10^{11}$
26	$CH_3CHC* + \# \rightarrow CH_3CC* + H\#$	deep	0.86	−0.62	$5.31 \cdot 10^{12}$	$1.51 \cdot 10^{12}$
27	$CH_3CCH* + \# \rightarrow CH_3CC* + H\#$	deep	0.92	+0.69	$5.82 \cdot 10^{11}$	$1.70 \cdot 10^{12}$
28	$C_3H_8* + * \rightarrow CH_3CH_2* + CH_3*$	cracking	3.23	+1.23	$2.93 \cdot 10^{11}$	$8.75 \cdot 10^{10}$
29	$CH_3CH_2CH_2* + * \rightarrow CH_3CH_2* + CH_2*$	cracking	2.90	+1.92	$4.39 \cdot 10^{12}$	$4.45 \cdot 10^{10}$
30	$CH_3CH_2CH_2* + * \rightarrow CH_3* + CH_2CH_2*$	cracking	2.32	+0.60	$4.79 \cdot 10^{13}$	$2.31 \cdot 10^{11}$
31	$CH_3CHCH_3* + * \rightarrow CH_3CH* + CH_3*$	cracking	2.95	+2.22	$2.74 \cdot 10^{12}$	$4.35 \cdot 10^{10}$
32	$CH_3CHCH_2* + * \rightarrow CH_3* + CH_2CH*$	cracking	3.29	+1.44	$4.71 \cdot 10^{11}$	$1.09 \cdot 10^{12}$
33	$CH_3CCH_3* + * \rightarrow CH_3C* + CH_3*$	cracking	2.55	+2.16	$2.66 \cdot 10^{12}$	$4.75 \cdot 10^{11}$
34	$CH_3CH_2CH* + * \rightarrow CH_3* + CH_2CH*$	cracking	3.20	−0.11	$2.77 \cdot 10^{12}$	$8.15 \cdot 10^{11}$
35	$CH_3CHCH* + * \rightarrow CH_3* + CHCH*$	cracking	2.79	+1.26	$4.09 \cdot 10^{12}$	$5.50 \cdot 10^{10}$
36	$CH_3CCH_2* + * \rightarrow CH_3* + CH_2C*$	cracking	1.68	+3.03	$1.07 \cdot 10^{13}$	$6.80 \cdot 10^{11}$
37	$CH_3CH_2C* + * \rightarrow CH_3* + CH_2C*$	cracking	2.76	−0.11	$1.45 \cdot 10^{13}$	$8.60 \cdot 10^{11}$
38	$CH_3CCH* + * \rightarrow CH_3* + CHC*$	cracking	3.14	+1.46	$4.38 \cdot 10^{11}$	$1.78 \cdot 10^{12}$
39	$CH_3CHC* + * \rightarrow CH_3* + CHC*$	cracking	3.13	+0.16	$1.42 \cdot 10^{13}$	$5.61 \cdot 10^{12}$
40	$C_2H_6* + \# \rightarrow CH_3CH_2* + H\#$	dehydr.	1.42	+0.76	$6.20 \cdot 10^{11}$	$1.43 \cdot 10^{13}$
41	$CH_3CH_2* + \# \rightarrow CH_2CH_2* + H\#$	dehydr.	1.42	+0.21	$8.24 \cdot 10^{11}$	$2.07 \cdot 10^{11}$
42	$CH_3CH_2* + \# \rightarrow CH_3CH* + H\#$	deep	1.99	+1.72	$3.53 \cdot 10^{12}$	$1.28 \cdot 10^{12}$
43	$CH_2CH_2* + \# \rightarrow CH_2CH* + H\#$	dehydr.	1.28	+0.88	$1.66 \cdot 10^{11}$	$2.62 \cdot 10^{12}$
44	$CH_3CH* + \# \rightarrow CH_3C* + H\#$	deep	1.59	+1.83	$2.74 \cdot 10^{12}$	$9.72 \cdot 10^{12}$
45	$CH_3CH* + \# \rightarrow CH_2CH* + H\#$	deep	0.60	−0.63	$1.88 \cdot 10^{11}$	$2.07 \cdot 10^{12}$
46	$CH_2CH* + \# \rightarrow CH_2C* + H\#$	deep	1.86	+1.63	$1.59 \cdot 10^{13}$	$7.85 \cdot 10^{12}$
47	$CH_2CH* + \# \rightarrow CHCH* + H\#$	dehydr.	1.47	+0.72	$3.61 \cdot 10^{12}$	$1.18 \cdot 10^{11}$
48	$CH_3C* + \# \rightarrow CH_2C* + H\#$	deep	0.17	−0.83	$4.03 \cdot 10^{12}$	$6.19 \cdot 10^{12}$
49	$CHCH* + \# \rightarrow CHC* + H\#$	deep	0.70	+0.58	$2.15 \cdot 10^{11}$	$9.81 \cdot 10^{12}$
50	$CH_2C* + \# \rightarrow CHC* + H\#$	deep	0.55	−0.32	$6.39 \cdot 10^{12}$	$1.92 \cdot 10^{13}$
51	$CHC* + \# \rightarrow CC* + H\#$	deep	1.99	+3.04	$1.29 \cdot 10^{12}$	$8.21 \cdot 10^{11}$
52	$C_2H_6* + * \rightarrow CH_3* + CH_3*$	cracking	3.13	+1.11	$2.83 \cdot 10^{10}$	$1.58 \cdot 10^{12}$
53	$CH_3CH_2* + * \rightarrow CH_3* + CH_2*$	cracking	2.75	+1.89	$7.65 \cdot 10^{11}$	$1.67 \cdot 10^{11}$
54	$CH_3CH* + * \rightarrow CH_3* + CH*$	cracking	2.53	+2.27	$3.22 \cdot 10^{11}$	$6.21 \cdot 10^{11}$
55	$CH_3C* + * \rightarrow CH_3* + C*$	cracking	2.30	+2.03	$2.92 \cdot 10^{12}$	$5.84 \cdot 10^{12}$
56	$CH_4* + \# \rightarrow CH_3* + H\#$	deep	1.42	+0.78	$3.65 \cdot 10^{10}$	$2.03 \cdot 10^{13}$
57	$CH_3* + \# \rightarrow CH_2* + H\#$	deep	1.98	+1.54	$3.28 \cdot 10^{12}$	$1.73 \cdot 10^{12}$
58	$CH_2* + \# \rightarrow CH* + H\#$	deep	2.31	+2.11	$9.88 \cdot 10^{11}$	$3.16 \cdot 10^{12}$
59	$CH* + \# \rightarrow C* + H\#$	deep	1.86	+2.01	$1.45 \cdot 10^{12}$	$5.30 \cdot 10^{12}$
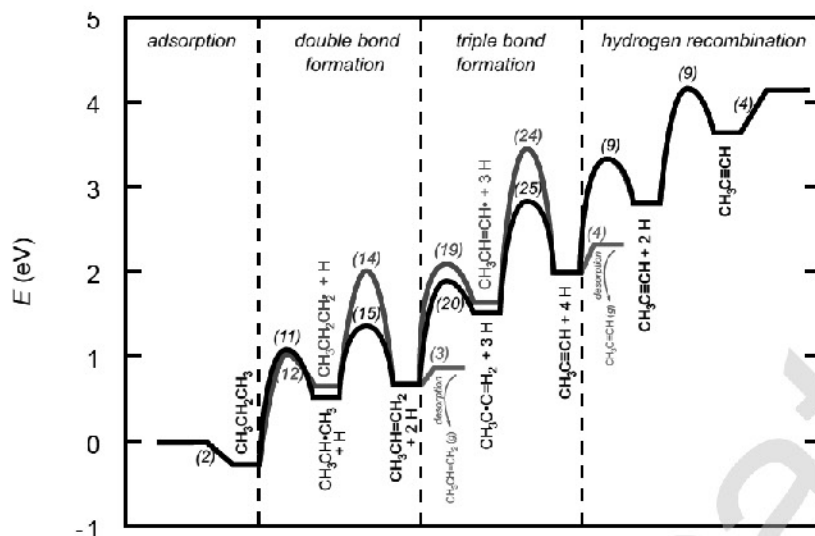
Figure 6: Potential energy surface for propane dehydrogenation over $Cr_2O_3(0001)$ without the reactions of deep dehydrogenation. Stable compounds, which can desorb, are written in bold. All values are in eV. Reactions numbered as in Table 2.

Lateral interactions are an often neglected yet important aspect of the reaction kinetics. In Table 3, we list the calculated lateral interactions of the intermediates. Due to the sheer number of intermediates, we limit the calculation to the hydrogen-containing pairs. This assumption is warranted by the structure of the catalyst. Carbon-containing intermediates bind to the exposed chromium atoms on the surface, which are far enough apart that their lateral interactions are negligible. The interaction between two co-adsorbed propyne molecules was 0.02 eV, which is lower than the accuracy of the DFT method. Hydrogen atoms, however, bind to oxygen atoms, which are in close vicinity to the chromium atoms. As shown in Table 3, these lateral interactions matter.

For radicals with several lone electrons the lateral interaction with hydrogen atoms is favourable. For instance, the interaction $CH_3CC\ldots H$ is -0.27 eV, for $CH_3C\ldots H$ already -0.81 eV and for $CC\ldots H$ even -1.04 eV. This also explains why for some elementary reactions in Table 2 the reaction energy seems higher than the barrier: the reported reaction energies in the table are relative to infinitely separated products and/or reactants. The aforementioned lateral interactions are included in the kinetic modelling (see below) as a typical first nearest neighbour correction. The lateral interactions between the hydrocarbon

fragments are negligible (for instance 0.01 eV for $CH_3CC^*\ldots CH_3CC^*$) because Cr sites are sufficiently distant from each other.

Table 3: Lateral interactions of the adsorbed species (in eV) with hydrogen.

species 1	species 2	E_{int}
H	H	−0.24
C_3H_8	H	+0.01
$CH_3CH_2CH_2$	H	+0.08
CH_3CHCH_3	H	+0.06
CH_3CH_2CH	H	−0.01
CH_3CHCH_2	H	+0.03
CH_3CCH_3	H	−0.10
CH_3CH_2CH	H	−0.25
CH_3CHCH	H	+0.07
CH_3CCH_2	H	+0.03
CH_3CHC	H	−0.36
CH_3CCH	H	+0.02
CH_3CC	H	−0.27
C_2H_6	H	0.00
CH_3CH_2	H	+0.06
CH_3CH	H	−0.24
CH_2CH_2	H	+0.02
CH_3C	H	−0.81
CH_2CH	H	−0.06
CH_2C	H	−0.26
$CHCH$	H	+0.08
CHC	H	−0.27
CC	H	−1.04
CH_4	H	0.00
CH_3	H	+0.02
CH_2	H	−0.50
CH	H	−0.48
C	H	−0.89

Kinetic modelling

Kinetic parameters

In Figure 7a, we plot the temperature dependence of the rate of propane and propene (also included are ethane and ethene) dehydrogenation, which is measured as a turnover frequency (TOF). Plotting the TOFs against the inverse temperature (Arrhenius plot), we obtain the apparent activation barriers. At 1 bar of pure propane in the reaction mixture, the barrier is 1.37 eV, which is remarkably close to the experimental value of 1.47 eV (see the last section).[30] The barrier of propene dehydrogenation is somewhat higher, *i.e.* 1.57 eV, and the reaction rate is for approximately an order of magnitude slower. Ethane and ethene exhibit a very slow conversion. The order of the reaction with respect to the products is determined from Figure 7b. Plotting the TOF's as a function of pressure on a logarithmic scale reveals the reaction order to be ∼1 for all dehydrogenations.
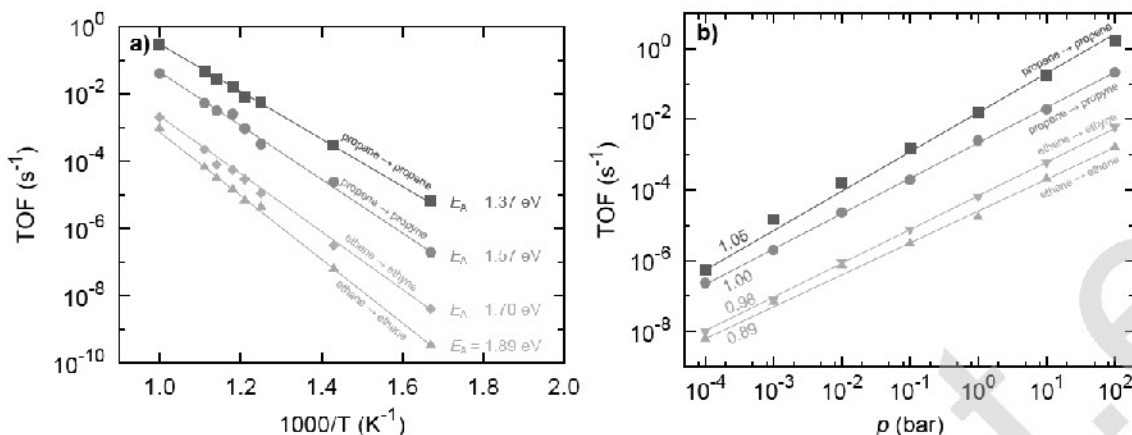
17

Figure 7: (a) Turnover frequencies (TOF) for propane, propene, ethane and ethene dehydrogenation as a function of temperature at 1 bar reactant (b) and as a function of pressure at 850 K (right).

Effects of hydrogen

Hydrogen is a by-product of the non-oxidative dehydrogenation. Thus, its build-up in the reaction stream could have deleterious effects on the reaction rate. In Figure 8a, the TOFs for propane and propene dehydrogenation at 850 K and a constant reactant pressure (1 bar of propane) are shown as a function of hydrogen pressure in the mixture. The effect exists but is not remarkable, *i.e.* the reaction is zero-order with respect to hydrogen except at extremely high pressure. The reason is two-fold. First, hydrogen occupies different sites than the hydrocarbons, not interfering in their interconverisons. Secondly, the coverage of molecular and atomic hydrogen on the catalyst is low, as shown in Figure 8b. Even at exceedingly high hydrogen pressures (10 bar H_2 and 1 bar of propane), the coverage of both hydrogen species *combined* is below 5 %. Thus, an increased gaseous concentration of hydrogen does not saturate the catalyst sites, leaving enough vacant sites for the reaction to proceed.
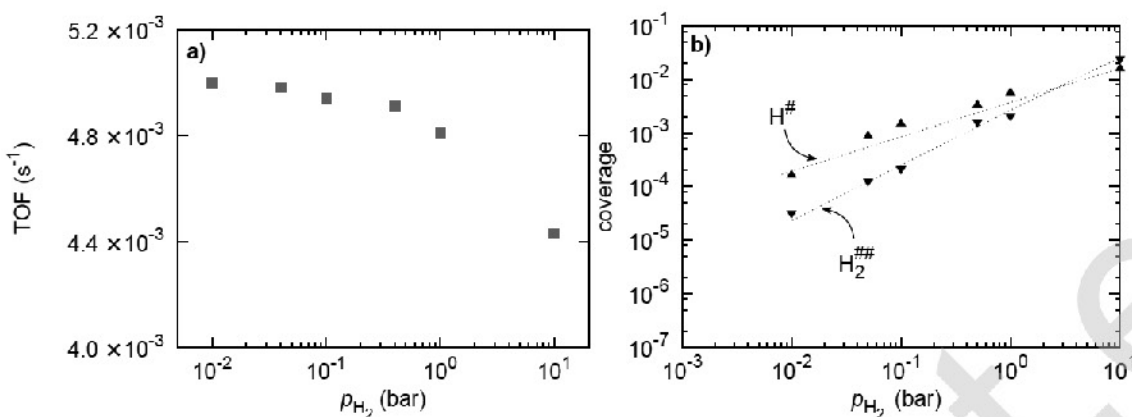
18

Figure 8: (a) Turnover frequencies (TOF) for propane at 850 K and 1 bar reactant as a function of the partial pressure of hydrogen in the stream. (b) Hydrogen coverage at 850 K and 1 bar propane as a function of hydrogen pressure.

Effects of contaminants

The build-up of propene or propyne in the reaction mixture, however, *can* have an effect on the product ratio. Therefore, we first investigate the case with the total reactant pressure of 1 bar and varying fractions of propane and propene at 850 K. In Figure 9a we plot the TOFs for propane and propene as a function of the mixture composition. Although the rate of propene dehydrogenation is lower, the selectivity also drops. At 70 % of propene in the mixture, the selectivity drops to 50 %. This shows that the selectivity drop is only relevant at a high partial pressure of propyne. Understandably, as the fraction (and thus partial pressure) of propane drops, the reaction rate is also suppressed.

With kinetic simulations, we can investigate the effect of contaminants in a *ceteris paribus* scenario. In Figure 9b, the propane pressure is kept constant at 1 bar and propene or propyne is added to the system. According to le Chatelier's principle, the turnover frequency (TOF) for propane dehydrogenation is decreased upon the addition of propene or propyne, which are the product of the reaction. Even small amounts of propene decrease the reaction but by a factor of 2.7 at the most. Propyne, however, is much more strongly bound to the surface and consequently competes with propane successfully, killing the reaction already in
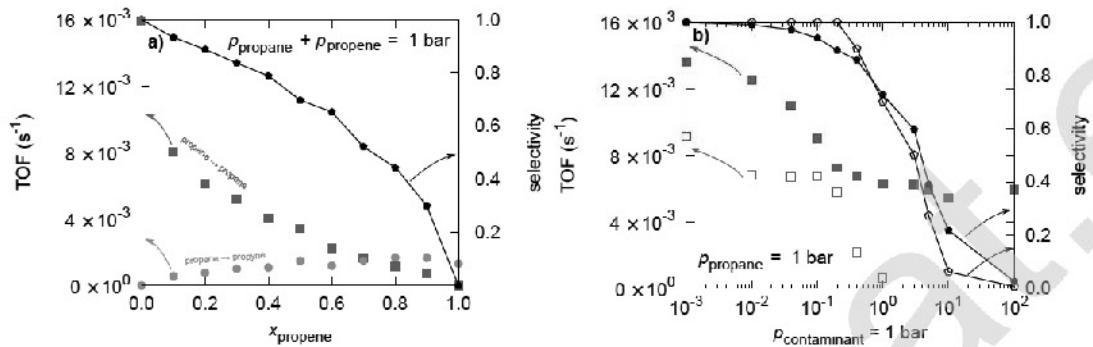
the percent range.

Figure 9: (a) TOF and selectivity of propane dehydrogenation as a function of propane fraction at 850 K and 1 bar total pressure ($p_{\text{propane}} + p_{\text{propene}}$). (b) TOF for propane dehydrogenation at 850 K and 1 bar propane as a function of added propene (solid symbols) or propyne (empty symbols).

This effect is responsible for a much more pronounced slowdown of *propene* dehydrogenation when propyne is present in the mixture. In Figure 10a, the TOF for this reaction is shown at 850 K as a function of added propyne when the partial pressure of propene is kept constant at 1 bar. As the fraction of propyne grows, the TOF decreases for more than two orders of magnitude. The underlying reason is shown in Figure 10b, where the surface coverages of propene, propyne and CH_3CC^* for the same sets of conditions is plotted. While the coverage of propene remains low at 1 bar, propyne and CH_3CC^* quickly saturate the catalyst. While propyne reversibly decreases the catalyst activity, CH_3CC^* represents an irreversible poison, as shown later on.
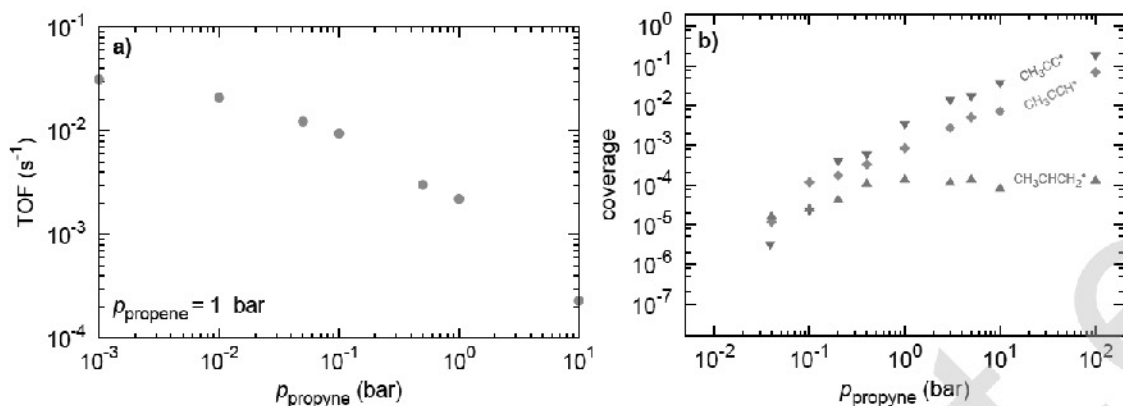
20

Figure 10: (a) TOF for propene dehydrogenation at 850 K and 1 bar propene as a function of added propyne. (b) Surface coverage during propene dehydrogenation at 850 K and 1 bar propene as a function of added propyne.

Deactivation

Lastly, we focus on the deactivation of the catalyst, which is a grave problem in all dehydrogenation reactions. While cracking decreases the selectivity of the reaction and prevents increasing its rate by (excessively) cranking up the temperature, coking irreversibly damages the catalyst. From Figure 11, where we plot the event frequency of the individual elementary reaction steps at 900 K and 1500 K (at 1 bar of propane), we can ascertain that the system is well-equilibrated and investigate the principle reaction steps. Further analysis shows the most probable pathway of dehydrogenation. Propane is predominantly dehydrogenated first on the secondary carbon atom and then on the terminal carbon atom. A smaller amount of the ensuing propene follows the same pattern to yield propyne. The overall most probable reaction pathway is thus $C_3H_8 \rightarrow CH_3CHCH_3 \rightarrow CH_3CHCH_2 \rightarrow CH_3CCH_2 \rightarrow CH_3CCH$.
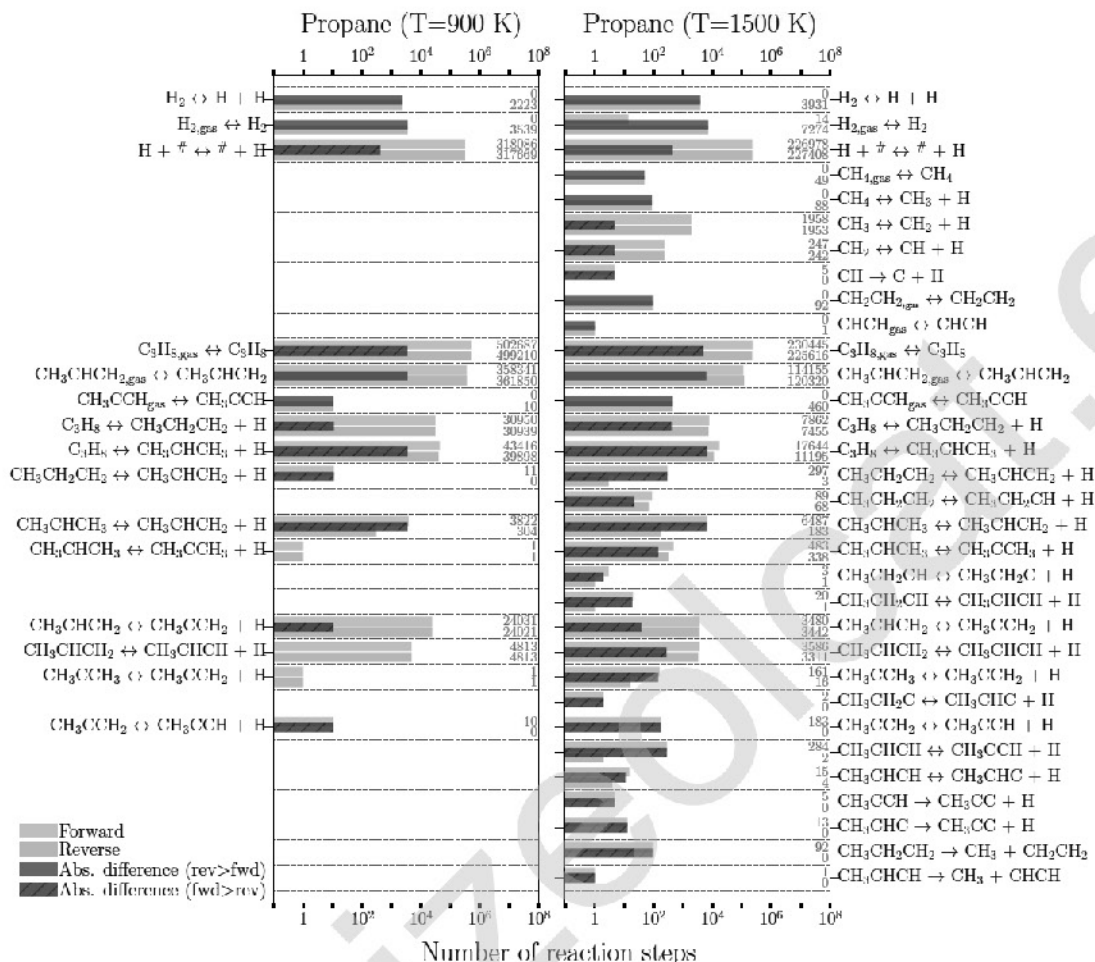
Figure 11: Event frequency for all elementary steps in the reaction network at 900 K (left) and 1500 K (right) and 1 bar reactant for propane dehydrogenation.

At the lower temperature, there is no craking within the simulated timeframe. To make the effect of catalyst more visible at achievable timescales, the simulation was run at 1500 K, as well. There we can see that the simulation visits the whole configuration space, with almost all postulated steps occurring. This results in the formation of CH_4, C_2H_6, CH_2CH_2 and CHCH. Moreover, considerable coking occurs, which we detail in Figure 12 and Table 4.

Only CH_3CC^* and C^* form in non-negligible amounts. They represent mechanistic dead-ends, being unable to react further. CH_3CC^* is tightly bound on top of chromium atoms in an upright position, while C^* has interacts strongly with an adjacent H^*, stabilizing its

22

Table 4: Apparent kinetic parameters for coking/catalyst deactivation.

reaction	A (s^{-1})	E_A (eV)
CH$_3$CC* formation	$1.72 \cdot 10^{10}$	2.88
C* formation	$1.96 \cdot 10^9$	2.67
catalyst deactivation	$1.66 \cdot 10^{10}$	2.82

formation. In Figure 12a, the Arrhenius plot for the formation of these species and the deactivation of the catalyst is shown. A temporal evolution of the catalytic surface is shown in Figure 12b, where the formation of the said species and the decrease of vacant sites (and thus activity) of the catalyst can be followed. In 12c, a snapshot of the catalytic surface upon considerable coke formation is shown.
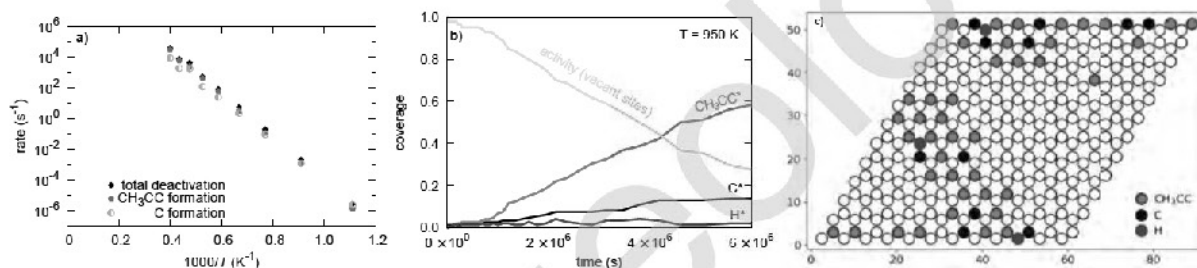

Figure 12: (a) Arrhenius plot for catalyst deactivation at 5 bar propane. (b) Temporal evolution of the catalyst at 950 K at 5 bar propane. (c) A lattice snapshot at 950 K after $3 \cdot 10^6$ seconds.

Putting it into perspective

Direct comparison of *ab initio* modelling results with experiments is difficult on account of several assumptions that are unattainable in experiments (a well-defined defect-free crystal lattice, its immutability, constant pressure and temperature, no formation of side products *etc.*). Nevertheless, first-principle insight is informative as it yields additional information about the mechanism and allows for a controlled investigation of the contribution of different factors. Despite fundamental differences in the set-up, we draw parallels to an experimental study.

Suzuki and Kaneko[30] investigated the (de)hydrogenation reaction in mixtures of propane,

propane + propene, propane + hydrogen, and propene + hydrogen at temperatures from 716 to 778 K over Cr_2O_3-Al_2O_3-K_2O. Although their reaction paths do not include elementary steps, our modelling agrees with their experimental data. The experimentally determined adsorption energy of propane was measured to be -10 kcal mol^{-1} (-0.43 eV), which is consistent with our value of -0.36 eV. We can attribute the small discrepancy to a different system, as the experimental catalyst also included Al_2O_3 and K_2O, and to notoriously bad description of the van der Waals interactions by DFT, which was compensated for using the Grimme D3 method. The activation barrier for propane dehydrogenation was discovered to be 33.9 kcal mol^{-1} (1.47 eV), which is close to our *ab initio* value of 1.37 eV.

In their microkinetic model, Gascón et al.[36] lump the cracking reaction into $C_3H_8 \rightarrow CH_4 + C_2H_4$ with the activation barrier of (308 ± 14) kJ mol^{-1} (3.21 ± 0.15 eV), while they treat coking with a lumped description $C_3H_8 \rightarrow CH_{\frac{1}{2}} + \frac{13}{4}H_2$ and linear differential equations. However, on a microkinetic level cracking and coking are intricately linked as a C–C bond cleavage is a prerequisite and a common initial step for both. We described the catalyst deactivation in an Arrhenius fashion with the activation energy of 2.82 eV, which is resonably close to the experimental measurements.

Lastly, the experimentally observed effect of propene on the dehydrogenation of propane can be compared with our modelling data. Suzuki and Kaneko[30] noticed in their experiments that the TOF for propane dehydrogenation decreases when hydrogen is present. They noticed that the ratio $r^0/(r_0^0 - r^0)$ (the "slowndown" ratio) depends linearly on the pressure of propane, where r_0^0 is the reaction rate in the absence of propene, and r^0 is the reaction rate with the constant pressure of propene added. The ratio varies from 1.0–2.4. In our model, the slowdown factor plateaus at ~ 2.7 when the pressure of propene exceeds that of propane (Figure 9b).

Conclusions

In this work, non-oxidative propane dehydrogenation to propene and propyne over a heterogeneous chromium oxide catalyst was studied. The catalyst was modelled as a (0001) slab of Cr_2O_3 which is the most stable surface termination of chromia. A comprehensive reaction network pathway of hydrogen abstraction from propane and the ensuing compounds was postulated, which included all possible elementary reaction steps yielding propene and propyne. The steps responsible for coking (formation of C^*), cracking (yielding CH_4, CH_2CH_2) and catalyst deactivation (CH_3CC^*) were also included. DFT+U calculations were used to find the most stable adsorption sites on the catalyst for each intermediate. Based on extensive literature data and comparisons between experiments and theory, the PW91 functional with the Hubbard approach ($D-J = 5\,eV$) was selected as the best compromise between accuracy and computational cost for the electronic structure calculations.

The adsorption energies for molecular H_2 and satured hydrocarbons are very low, resulting in no noticeable surface build-up. Any adsorbed hydrogen or propane are quickly consumed. This also means that there are no specific adsorption sites for these molecules. Propene and propyne (and their C_2 counterparts), however, are bound more strongly and assume a preferential top position over Cr atoms. In all cases, the effect is purely electronic as the distortion contribution to the adsorption energies remains negligible. The coverage with propene is also low, while propyne has the propensity to attain noticeable coverages on the catalyst at elevated pressures (above 0.1 bar at normal operating temperatures).

A kinetic model was built from the reaction network pathway proposed in the model. Using the transition state theory, the rates for every elementary reaction were calculated as a function of temperature and pressure (for Eley-Rideal adsorptions). A closer inspection of the reaction barriers suggested $C_3H_8 \rightarrow CH_3CHCH_3 \rightarrow CH_3CHCH_2 \rightarrow CH_3CCH_2 \rightarrow CH_3CCH$ to be the predominant reaction path. For cracking, $CH_3CH_2CH_2 \rightarrow CH_3CH_2 + CH_2$ was the most important step. Deactivation of the catalyst is a consequence of coking and formation of a relatively inert CH_3CC^* species.

Kinetic modelling with the kMC at different temperatures (700 1000 °C), pressures (up to 10 bar) and inlet mixture compositions revealed additional kinetic parameters. Moreover, we showed that due to low surface coverage of hydrogen and propene, their presence does not significantly impede propane dehydrogenation. The reaction rate decreases for a factor up to 2.7, while the selectivity also drops. Propyne has a much stronger effect on the dehydrogenation of propane or propene. When its partial pressure increases sufficiently to saturate the catalyst, it slows down the dehydrogenation considerably. The effect is exponential, representing a 100-fold decrease in the TOF as the fraction of propyne increases from 0 to 90 %. Greater pressure of propyne also additionally accelerates the build-up of non-active species on the surface, poisoning the catalyst.

Based on our results, we explain why and how chromium oxide represents a good catalyst for propane dehydrogenation. In practical applications, it is usually doped with nobel and alkali metals, often supported on zeolites. Our modelling indicates which reaction steps represent the bottleneck in the reaction rate and which steps yield the unwanted side reaction. For modelling on higher scales (reactor level), the reaction network must be reduced to a simpler rate law. This work shows which elementary reactions must be studied in detail when developing or fine-tuning the catalysts for this reaction.

Acknowledgement

References

(1) McGlade, C.; Ekins, P. The geographical distribution of fossil fuels unused when limiting global warming to 2 °C. *Nature* **2015**, *517*, 187–190.

(2) Sattler, J. J. H. B.; Ruiz-Martinez, J.; Santillan-Jimenez, E.; Weckhuysen, B. M. Catalytic Dehydrogenation of Light Alkanes on Metals and Metal Oxides. *Chem. Rev.* **2014**, *114*, 10613–10653.

(3) Bruijnincx, P. C. A.; Weckhuysen, B. M. Shale Gas Revolution: An Opportunity for the Production of Biobased Chemicals? *Angewandte Chemie International Edition* **2013**, *52*, 11980–11987.

(4) Atanga, M. A.; Rezaei, F.; Jawad, A.; Fitch, M.; Rownaghi, A. A. Oxidative dehydrogenation of propane to propylene with carbon dioxide. *Applied Catalysis B: Environmental* **2018**, *220*, 429–445.

(5) Wang, L.-C.; Zhang, Y.; Xu, J.; Diao, W.; Karakalos, S.; Liu, B.; Song, X.; Wu, W.; He, T.; Ding, D. Non-oxidative dehydrogenation of ethane to ethylene over ZSM-5 zeolite supported iron catalysts. *Applied Catalysis B: Environmental* **2019**, *256*, 117816.

(6) Han, S.; Otroshchenko, T.; Zhao, D.; Lund, H.; Rodemerck, U.; Linke, D.; Gao, M.; Jiang, G.; Kondratenko, E. V. Catalytic non-oxidative propane dehydrogenation over promoted Cr-Zr-Ox: Effect of promoter on propene selectivity and stability. *Catalysis Communications* **2020**, 105956.

(7) Cao, L.; Dai, P.; Zhu, L.; Yan, L.; Chen, R.; Liu, D.; Gu, X.; Li, L.; Xue, Q.; Zhao, X. Graphitic carbon nitride catalyzes selective oxidative dehydrogenation of propane. *Applied Catalysis B: Environmental* **2020**, *262*, 118277.

(8) Cavani, F.; Ballarini, N.; Cericola, A. Oxidative dehydrogenation of ethane and

propane: How far from commercial implementation? *Catalysis Today* **2007**, *127*, 113 131.

(9) Gianotti, E.; Taillades-Jacquin, M.; Álvaro Reyes-Carmona.; Taillades, G.; Rozière, J.; Jones, D. J. Hydrogen generation via catalytic partial dehydrogenation of gasoline and diesel fuels. *Applied Catalysis B: Environmental* **2016**, *185*, 233 – 241.

(10) Faria, W. L. S.; Dieguez, L. C.; Schmal, M. Autothermal reforming of propane for hydrogen production over Pd/CeO2/Al2O3 catalysts. *Applied Catalysis B: Environmental* **2008**, *85*, 77 85.

(11) Sokolov, S.; Stoyanova, M.; Rodemerck, U.; Linke, D.; Kondratenko, E. V. Comparative study of propane dehydrogenation over V-, Cr-, and Pt-based catalysts: Time on-stream behavior and origins of deactivation. *Journal of Catalysis* **2012**, *293*, 67 – 75.

(12) Schäfer, R.; Noack, M.; Kölsch, P.; Stöhr, M.; Caro, J. Comparison of different catalysts in the membrane-supported dehydrogenation of propane. *Catalysis Today* **2003**, *82*, 15 – 23, 5th International Conference on Catalysis in Membrane Reactors.

(13) Shan, Y.; Sui, Z.; Zhu, Y.; Chen, D.; Zhou, X. Effect of steam addition on the structure and activity of Pt–Sn catalysts in propane dehydrogenation. *Chemical Engineering Journal* **2015**, *278*, 240 – 248, Tailoring Sustainability through Chemical Reaction Engineering.

(14) Liu, X.; Lang, W.-Z.; Long, L.-L.; Hu, C.-L.; Chu, L.-F.; Guo, Y.-J. Improved catalytic performance in propane dehydrogenation of PtSn/γ-Al$_2$O$_3$ catalysts by doping indium. *Chemical Engineering Journal* **2014**, *247*, 183 – 192.

(15) Shen, L.-L.; Xia, K.; Lang, W.-Z.; Chu, L.-F.; Yan, X.; Guo, Y.-J. The effects of calcination temperature of support on PtIn/Mg(Al)O catalysts for propane dehydrogenation reaction. *Chemical Engineering Journal* **2017**, *324*, 336 – 346.

(16) Zhao, Z.-J.; Chiu, C.-c.; Gong, J. Molecular understandings on the activation of light hydrocarbons over heterogeneous catalysts. *Chem. Sci.* **2015**, *6*, 4403 4425.

(17) Gascón, J.; Téllez, C.; Herguido, J.; Menéndez, M. A two-zone fluidized bed reactor for catalytic propane dehydrogenation. *Chemical Engineering Journal* **2005**, *106*, 91 – 96.

(18) Vernikovskaya, N.; Savin, I.; Kashkin, V.; Pakhomov, N.; Ermakova, A.; Molchanov, V.; Nemykina, E.; Parahin, O. Dehydrogenation of propane–isobutane mixture in a fluidized bed reactor over Cr_2O_3/Al_2O_3 catalyst: Experimental studies and mathematical modelling. *Chemical Engineering Journal* **2011**, *176-177*, 158 – 164, XIX 4 International Conference on Chemical Reactors (CHEMREACTOR-19).

(19) Shelepova, E.; Vedyagin, A.; Mishakov, I.; Noskov, A. Mathematical modeling of the propane dehydrogenation process in the catalytic membrane reactor. *Chemical Engineering Journal* **2011**, *176-177*, 151 – 157, X1X 4 International Conference on Chemical Reactors (CHEMREACTOR-19).

(20) Wang, G.; Zhang, H.; Wang, H.; Zhu, Q.; Li, C.; Shan, H. The role of metallic Sn species in catalytic dehydrogenation of propane: Active component rather than only promoter. *Journal of Catalysis* **2016**, *344*, 606 – 608.

(21) Yang, M.-L.; Zhu, Y.-A.; Fan, C.; Sui, Z.-J.; Chen, D.; Zhou, X.-G. DFT study of propane dehydrogenation on Pt catalyst: effects of step sites. *Phys. Chem. Chem. Phys.* **2011**, *13*, 3257 3267.

(22) Yang, M.-L.; Zhu, J.; Zhu, Y.-A.; Sui, Z.-J.; Yu, Y.-D.; Zhou, X.-G.; Chen, D. Tuning selectivity and stability in propane dehydrogenation by shaping Pt particles: A combined experimental and DFT study. *Journal of Molecular Catalysis A: Chemical* **2014**, *395*, 329 – 336.

(23) Vajda, S.; Pellin, M. J.; Greeley, J. P.; Marshall, C. L.; Curtiss, L. A.; Ballentine, G. A.; Elam, J. W.; Catillon-Mucherie, S.; Redfern, P. C.; Mehmood, F.; Zapol, P. Sub-

nanometre platinum clusters as highly active and selective catalysts for the oxidative dehydrogenation of propane. *Nature Materials* **2009**, *8*, 213 216.

(24) Li, Q.; Sui, Z.; Zhou, X.; Chen, D. Kinetics of propane dehydrogenation over Pt-Sn/Al2O3 catalyst. *Applied Catalysis A: General* **2011**, *398*, 18 26.

(25) Yang, M.-L.; Zhu, Y.-A.; Zhou, X.-G.; Sui, Z.-J.; Chen, D. First-Principles Calculations of Propane Dehydrogenation over PtSn Catalysts. *ACS Catal.* **2012**, *2*, 1247 1258.

(26) Yang, M.-L.; Zhu, Y.-A.; Fan, C.; Sui, Z.-J.; Chen, D.; Zhou, X.-G. Density functional study of the chemisorption of C1, C2 and C3 intermediates in propane dissociation on Pt(111). *Journal of Molecular Catalysis A: Chemical* **2010**, *321*, 42 49.

(27) Lian, Z.; Ali, S.; Liu, T.; Si, C.; Li, B.; Su, D. S. Revealing the Janus Character of the Coke Precursor in the Propane Direct Dehydrogenation on Pt Catalysts from a kMC Simulation. *ACS Catalysis* **2018**, *8*, 4694 4704.

(28) Nykänen, L.; Honkala, K. Density Functional Theory Study on Propane and Propene Adsorption on Pt(111) and PtSn Alloy Surfaces. *J. Phys. Chem. C* **2011**, *115*, 9578 9586.

(29) Nykänen, L.; Honkala, K. Selectivity in Propene Dehydrogenation on Pt and Pt_3Sn Surfaces from First Principles. *ACS Catal.* **2013**, *3*, 3026 3030.

(30) Suzuki, I.; Kaneko, Y. Dehydrogenation of propane over chromia-alumina-potassium oxide catalyst. *Journal of Catalysis* **1977**, *47*, 239 248.

(31) Chang, Q.-Y.; Yin, Q.; Ma, F.; Zhu, Y.-A.; Sui, Z.-J.; Zhou, X.-G.; Chen, D.; Yuan, W.-K. Tuning Adsorption and Catalytic Properties of α-Cr_2O_3 and ZnO in Propane Dehydrogenation by Creating Oxygen Vacancy and Doping Single Pt Atom: A Comparative First-Principles Study. *Ind. Eng. Chem. Res.* **2019**, *58*, 10199–10209.

(32) Zhang, X.; Yue, Y.; Gao, Z. Chromium Oxide Supported on Mesoporous SBA-15 as Propane Dehydrogenation and Oxidative Dehydrogenation Catalysts. *Catalysis Letters* **2002**, *83*, 19–25.

(33) Mentasty, L. R.; Gorriz, O. F.; Cadus, L. E. Chromium Oxide Supported on Different Al_2O_3 Supports: Catalytic Propane Dehydrogenation. *Ind. Eng. Chem. Res.* **1999**, *38*, 396–404.

(34) Shee, D.; Sayari, A. Light alkane dehydrogenation over mesoporous Cr_2O_3/Al_2O_3 catalysts. *Applied Catalysis A: General* **2010**, *389*, 155 164.

(35) Nijhuis, T. A.; Tinnemans, S. J.; Visser, T.; Weckhuysen, B. M. Towards real-time spectroscopic process control for the dehydrogenation of propane over supported chromium oxide catalysts. *Chemical Engineering Science* **2004**, *59*, 5487 – 5492, ISCRE18.

(36) Gascón, J.; Téllez, C.; Herguido, J.; Menéndez, M. Propane dehydrogenation over a Cr_2O_3/Al_2O_3 catalyst: transient kinetic modeling of propene and coke formation. *Applied Catalysis A: General* **2003**, *248*, 105–116.

(37) Y., C. S.; Radzi,; R., S. N.; Maharon,; H., I.; Shafawi,; A., M. Kinetic model and Simulation Analysis for Propane Dehydrogenation in an Industrial Moving Bed Reactor. *International Journal of Chemical and Molecular Engineering* **2011**, *5*, 260 – 266.

(38) Kresse, G.; Hafner, J. Ab Initio Molecular Dynamics for Liquid Metals. *Phys. Rev. B* **1993**, *47*, 558–561.

(39) Kresse, G.; Hafner, J. Ab Initio Molecular-dynamics Simulation of the Liquid-metal–amorphous-semiconductor Transition in Germanium. *Phys. Rev. B* **1994**, *49*, 14251–14269.

(40) Kresse, G.; Furthmüller, J. Efficiency of Ab-initio Total Energy Calculations for Metals

and Semiconductors Using a Plane-wave Basis Set. *Comput. Mater. Sci.* **1996**, *6*, 15 50.

(41) Kresse, G.; Furthmüller, J. Efficient Iterative Schemes for Ab Initio Total-energy Calculations Using a Plane-wave Basis Set. *Phys. Rev. B* **1996**, *54*, 11169 11186.

(42) Perdew, J. P.; Wang, Y. Accurate and simple analytic representation of the electron-gas correlation energy. *Phys. Rev. B* **1992**, *45*, 13244–13249.

(43) Blöchl, P. E. Projector Augmented-wave Method. *Phys. Rev. B* **1994**, *50*, 17953 17979.

(44) Kresse, G.; Joubert, D. From Ultrasoft Pseudopotentials to the Projector Augmented-wave Method. *Phys. Rev. B* **1999**, *59*, 1758 1775.

(45) Dudarev, S. L.; Botton, G. A.; Savrasov, S. Y.; Humphreys, C. J.; Sutton, A. P. Electron-energy-loss spectra and the structural stability of nickel oxide: An LSDA+U study. *Phys. Rev. B* **1998**, *57*, 1505–1509.

(46) Rohrbach, A.; Hafner, J.; Kresse, G. Ab initio study of the (0001) surfaces of hematite and chromia: Influence of strong electronic correlations. *Phys. Rev. B* **2004**, *70*, 125426.

(47) Costa, D.; Garrain, P.-A.; Diawara, B.; Marcus, P. Biomolecule–Biomaterial Interaction: A DFT-D Study of Glycine Adsorption and Self-Assembly on Hydroxylated Cr_2O_3 Surfaces. *Langmuir* **2011**, *27*, 2747–2760, PMID: 21338116.

(48) Nigussa, K. N.; Borck, Ø.; Støvneng, J. Adsorption of H_2S on α-Cr_2O_3(0001) surfaces: A density functional theory investigation. *Corrosion Science* **2016**, *111*, 1–12.

(49) Maldonado, F.; Stashans, A. DFT modelling of hydrogen sulphide adsorption on α-Cr_2O_3 (0001) surface. *Surface Science* **2016**, *647*, 78 – 83.

(50) Grimme, S.; Antony, J.; Ehrlich, S.; Krieg, H. A consistent and accurate ab initio parametrization of density functional dispersion correction (DFT-D) for the 94 elements H-Pu. *The Journal of Chemical Physics* **2010**, *132*, 154104.

(51) Jónsson, H.; Mills, G.; Jacobsen, K. W. *Classical and Quantum Dynamics in Condensed Phase Simulations*, 1st ed.; World Scientific, 1998.

(52) Xiao, P.; Sheppard, D.; Rogal, J.; Henkelman, G. Solid-state Dimer Method for Calculating Solid-solid Phase Transitions. *J. Chem. Phys.* **2014**, *140*, 174104.

(53) Kästner, J.; Sherwood, P. Superlinearly Converging Dimer Method for Transition State Search. *J. Chem. Phys.* **2008**, *128*, 014106.

(54) Heyden, A.; Bell, A. T.; Keil, F. J. Efficient Methods for Finding Transition States in Chemical Reactions: Comparison of Improved Dimer Method and Partitioned Rational Function Optimization Method. *J. Chem. Phys.* **2005**, *123*, 224101.

(55) Henkelman, G.; Jónsson, H. A Dimer Method for Finding Saddle Points on High Dimensional Potential Surfaces Using Only First Derivatives. *J. Chem. Phys.* **1999**, *111*, 7010 7022.

(56) Gao, J.; Zheng, Y.; Tang, Y.; Jehng, J.-M.; Grybos, R.; Handzlik, J.; Wachs, I. E.; Podkolzin, S. G. Spectroscopic and Computational Study of Cr Oxide Structures and Their Anchoring Sites on ZSM-5 Zeolites. *ACS Catalysis* **2015**, *5*, 3078 3092.

(57) Makov, G.; Payne, M. C. Periodic Boundary Conditions in Ab Initio Calculations. *Phys. Rev. B* **1995**, *51*, 4014–4022.

(58) Neugebauer, J.; Scheffler, M. Adsorbate-substrate and Adsorbate-adsorbate Interactions of Na and K Adlayers on Al(111). *Phys. Rev. B* **1992**, *46*, 16067–16080.

(59) Stamatakis, M.; Vlachos, D. G. A Graph-theoretical Kinetic Monte Carlo Framework for On-lattice Chemical Kinetics. *J. Chem. Phys.* **2011**, *134*, 214115.

(60) Nielsen, J.; d'Avezac, M.; Hetherington, J.; Stamatakis, M. Parallel Kinetic Monte Carlo Simulation Framework Incorporating Accurate Models of Adsorbate Lateral Interactions. *J. Chem. Phys.* **2013**, *139*, 224706.

(61) Pineda, M.; Stamatakis, M. Beyond Mean-field Approximations for Accurate and Computationally Efficient Models of On-lattice Chemical Kinetics. *J. Chem. Phys.* **2017**, *147*, 024105.

(62) Vignola, E.; Steinmann, S. N.; Vandegehuchte, B. D.; Curulla, D.; Stamatakis, M.; Sautet, P. A Machine Learning Approach to Graph-theoretical Cluster Expansions of the Energy of Adsorbate Layers. *J. Chem. Phys.* **2017**, *147*, 054106.

(63) Stamatakis, M.; Vlachos, D. G. Equivalence of On-lattice Stochastic Chemical Kinetics with the Well-mixed Chemical Master Equation in the Limit of Fast Diffusion. *Comput. Chem. Eng.* **2011**, *35*, 2602 − 2610.

Graphical TOC Entry